ACI STRUCTURAL JOURNAL TECHNICAL PAPER

Title No. 115-S88

Modeling of Sliding Behavior of Unbonded Tendons in Post-Tensioned Concrete Members

by Yu Huang and Thomas H.-K. Kang

This paper discusses a nonlinear finite element formulation comprising contact and engineering elements in modeling post-tensioned concrete members. The study focuses on modeling of the sliding behavior observed in post-tensioned tendons. Detailed discussion is presented for the modified node-to-segment contact formulation, by which the bonding interface is discretized and physically modeled. Perfectly unbonded, partially bonded, and fully bonded conditions are considered by introducing frictionless and frictional contact. Post-tensioned tendons are modeled by the nonlinear truss element and are embedded into the nonlinear reinforced concrete beam element. The embedding element comprises elastic Euler beam element with very large stiffness. The nonlinear anchorage element and the prestressing procedure are also proposed to simplify and to properly model the complex jacking process. The proposed formulations were implemented in a nonlinear finite element code developed in MATLAB. Validation of the proposed formulations and implementations were carried out in several numerical studies. The proposed formulation performed with a reasonably good accuracy in reproducing global flexural behavior as well as predicting localized prestress loss and redistribution.

Keywords: contact formulation; friction; nonlinear finite element; post-tensioned concrete; sliding.

INTRODUCTION

Over the last few decades, the research community has been actively exploring the finite element method in modeling concrete and composite structures (Kang et al. 2009; Fagan et al. 2017). Post-tensioned (PT) structures, among many other types of structural systems, have frequently received attention from researchers in the past, yet present great difficulties for applying conventional finite element formulation to the modeling. The fundamental of successfully modeling different types of prestressed concrete systems (that is, pre-tensioned, bonded, and unbonded PT system) lies in the interface modeling between prestressing tendons and surrounding concrete or corresponding sheathings. In the case of pre-tensioned and bonded PT systems, strain compatibility is commonly assumed in the literature (that is, perfect bonding condition). However, it is a great challenge to model the unbonded PT system due to the strain incompatibility caused by potential tendon sliding through sheathings during the prestressing and service loading. The complication of boundary nonlinearity is therefore presented to the finite element researchers. The modeling approaches toward the bonding interface likely fall into three categories in literature. Studies that fall into the first category typically employ empirical equations and special procedures to determine strains of unbonded tendons (Kang and Scordelis 1980; Van Greunen and Scordelis 1983; Nikolic and Mihanovic 1997). Even though it provides some practical values in design, the lack of modeling flexibility limits its application. In the second category, link or spring elements are normally introduced to connect unbonded tendons and surrounding sheathings or concrete (El-Mezaini and Çıtıpıtıolu 1991; El-Mezaini et al. 1991; Vecchio et al. 2006; Huang et al. 2010). The link element is free of rotation in the plan of tendon profile, where small sliding is emulated. This approach, while permitting a unified treatment to the problem in the context of finite element analysis, attains only small rotation and sliding, as large rotations of link elements may lead to inaccurate balancing force due to prestress (Huang et al. 2010). The approaches in the third category are often a combination of using link elements and empirical relations to determine loss of prestress with partially bonded condition (Wu et al. 2001). An intuitive and promising avenue of modeling finite sliding, to the authors' knowledge, is to formulate the bonding interface as a contact problem. However, there are very few studies addressing contact modeling toward unbonded PT structures (Ellobody and Bailey 2008; Huang et al. 2010). The literature is particularly lackluster in exploring the combination of contact formulation and engineering elements applied to PT members. Research aiming to improve solution reliability and robustness in PT system design still leaves a lot to be desired. As a corollary, this study concentrates heavily on the development of an effective and practical nonlinear finite element formulation, where a reasonably accurate representation of PT tendon stress can also be obtained at any given bonding condition (that is, bonded, partially bonded, and unbonded PT tendons). The formulation is straightforward and built upon physical insights. It can be implemented with some fast, numerical routines to help design PT members in practice. Material and boundary nonlinearity is considered in the proposed two-dimensional (2-D) formulation. The framework, however, is sufficiently generic to be extended to three-dimensional (3-D) cases taking geometric nonlinearity into consideration.

Five types of elements are employed to assemble a complete PT member. The prestressing tendon and concrete hosting member of beam or slab are, respectively, discret-

ACI Structural Journal, V. 115, No. 4, July 2018.
MS No. S-2017-293.R1, doi: 10.14359/51702066, was received August 15, 2017, and reviewed under Institute publication policies.

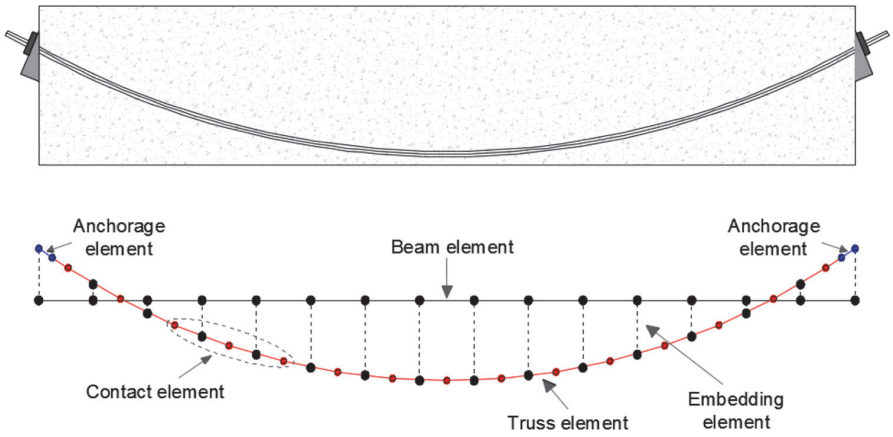

Fig. 1—Finite element discretization scheme for typical PT member.

ized via the two-node truss and two-node Euler-Bernoulli beam element considering material nonlinearity. The prestressing tendon sheathings are embedded into the elements of concrete beam through a series of embedding elements. The node-to-segment (NTS) contact formulation developed by Wriggers (2008) is the basis of interface modeling. To successfully adapt the NTS formulation to model sliding, some necessary modifications are discussed and introduced. An anchorage element is also developed to simplify the complex procedures of post-tensioning and to model the anchorage zone of prestressing tendons. The modified Newton-Raphson method with line search was employed to obtain numerical solutions. Finally, a series of numerical studies including analyses of two continuous PT beams, six simply supported PT beams, and two one-way PT slabs are presented to validate the proposed formulation.

RESEARCH SIGNIFICANCE

Many contact formulations and algorithms have been implemented and developed in commercial/non-commercial FEA codes. However, studies specifically centered on applying contact formulation to the modeling of PT members are lacking in the sense of developing accurate design solution with dispatch. To bridge this gap, a physical approach to model bonded, partially bonded, and unbonded PT members is developed with an emphasis on combining engineering element with contact formulation. In this study, the proposed modeling approach is provided in detail, along with the validation of several numerical studies. The framework is generic enough to be extended to other types of unbonded PT members.

TWO-DIMENSIONAL NONLINEAR FINITE ELEMENT FORMULATION OF PT BEAM

Discretization schemes

This section briefly discusses the discretization schemes employed to assemble a PT beam member. A typical PT beam is discretized into a series of engineering elements as shown in Fig. 1. The black thicker line represents the reference location of the element that discretizes the beam without prestressing tendons. The prestressing tendons are modeled via a series of first-order truss elements rendered as a red parabolic line in Fig. 1. The dotted lines represent the embedding elements that are, in fact, rigid beams or alternatively very stiff beams. The embedding elements ensure that the prestress-induced load and moment are appropriately transferred to the reference location of the PT beam. The anchorage element located at either end of the PT beam comprises two nodes. The first node is from the tendon element and the other node is from the adjacent embedding element (blue solid lines at the end of the beam in Fig. 1). A typical contact element consists of five nodes with 12 degrees of freedom. Among all five nodes, two are from a pair of adjacent embedding elements (or in the case of anchorage zone, one node from anchorage element and the other node from embedding element) and the remaining nodes belong to two nearby linear tendon elements with the middle shared node confined between the adjacent embedding elements; therefore, the middle shared node of tendon elements is constrained along the linear segment (sheathing) depicted by a straight line (dotted circle in Fig. 1). The proposed formulation also allows multiple nodes of tendon to be in contact with one line segment via constantly activating new and removing old contact elements through a contact search algorithm before every iteration. This treatment ensures that finely meshed tendon elements will still work well with coarsely meshed beam elements and vice versa. Based on the discretization schemes, a NTS contact formulation (Wriggers 2008) was employed. The NTS formulation is modified in this study to correct the artificial prestress deviation. The element development is presented in the next section.

Contact element

Kinematics of contact element—Figure 2 shows a contact element in detail where X_s, X_1, X_2, X_3, and X_4 denote the position vectors of the middle slave contact node (from tendon elements), the two master nodes of the contact segment (from embedding elements), and the two side tendon nodes adjacent to the middle slave contact node (from tendon elements) (also see the list of notations in Appendix A*. The tendon node (middle slave node) is constrained along the

*The Appendix is available at **www.concrete.org/publications** in PDF format, appended to the online version of the published paper. It is also available in hard copy from ACI headquarters for a fee equal to the cost of reproduction plus handling at the time of the request.

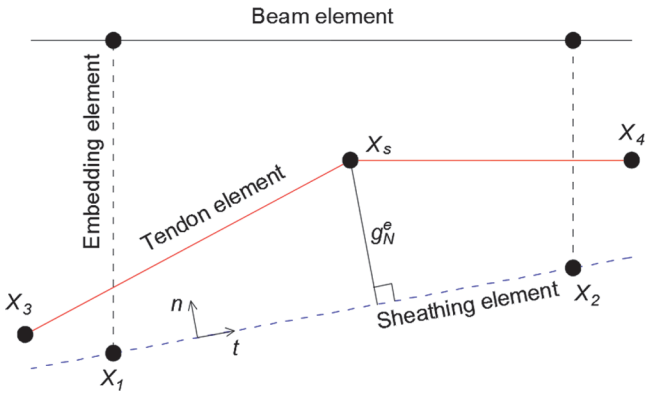

Fig. 2—Formulation of contact element.

straight line formed by the two master nodes (contact master segment). The distance between the slave node and master segment in the contact element e is derived as

$$g_n^e = \left[X_s - (1-\bar{\xi})X_1 - \bar{\xi}X_2 \right] \cdot n \tag{1}$$

where n is the unit normal vector with respect to the master segment, and $\bar{\xi}$ is the projection of the slave node onto the master segment in the master segment local coordinate as

$$\bar{\xi} = \frac{(X_s - X_1)\cdot t}{l_{ct}^e} \tag{2}$$

where t and l_{ct}^e, respectively, denote the unit tangential vector along the master segment and the length of the master segment. The function of slip motion (g_t^e) associated with contact element e is derived as

$$g_t^e = (\bar{\xi} - \xi_0) l_{ct}^e \tag{3}$$

where ξ_0 denotes the local surface coordinate of the slave node projected onto the master surface at the initial configuration. The variation of g_n^e and g_t^e are computed as

$$\delta g_n^e = \left[\delta d_s^e - (1-\bar{\xi})\delta d_1^e - \bar{\xi}\delta d_2^e \right] \cdot n \tag{4}$$

$$\begin{aligned} \delta g_t^e = &\left[\delta d_s^e - (1-\bar{\xi})\delta d_1^e - \bar{\xi}\delta d_2^e \right] \cdot t \\ &+ \frac{g_n^e [\delta d_2^e - \delta d_1^e] \cdot \boldsymbol{n}}{l_{ct}^e} + \frac{g_t^e [\delta d_2^e - \delta d_1^e] \cdot t}{l_{ct}^e} \end{aligned} \tag{5}$$

where δd_s^e, δd_1^e, and δd_2^e are, respectively, the virtual displacements of the slave node and the master nodes of the contact element e. Equations (4) and (5) represent the kinematic relations of the contact element proposed by Wriggers (2008). The finite element discretized form of the virtual work for a contact element is given as

$$\delta \prod = \delta g_n^e P_n^e + \delta g_t^e T_t^e \tag{6}$$

where P_n^e and T_t^e are the normal and tangential contact forces that are determined by the constitutive equation selected at

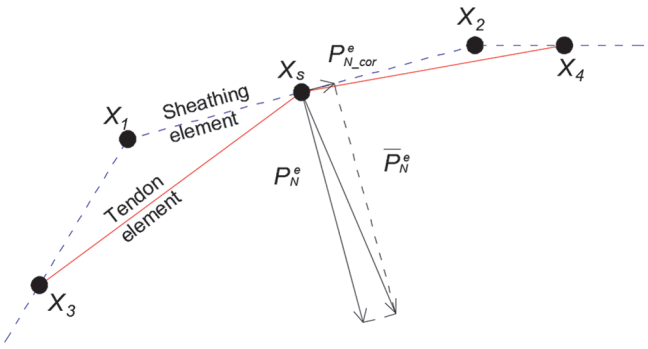

Fig. 3—Illustration of tangential correction force to eliminate artificial prestress loss or gain along tendon path.

the contact interface; and e represents the element label. In the next section, it is shown that the default NTS discretization scheme, unfortunately, introduces either artificial prestress loss or prestress gain due to that normal contact force is less likely aligned with the normal direction of prestressed tendon in the proposed discretized configuration. This is inevitable, as both prestressed tendons and sheathings are discretized into series of linear segments. Even though the nodes of tendon are constrained along the path of sheathing elements, the tendon element and the adjacent sheathing path most likely do not overlap, as illustrated in Fig. 3. Therefore, it is crucial to introduce a small correction force to align the normal contact force (P_n^e) with the normal direction of the tendon at every contact slave node. Note that the normal direction of tendon at each node is defined as the direction such that any force exerted along the direction on that node can be decomposed into two equal load vectors following the directions of the two adjacent tendon segments (that is, the "middle" vector between the two adjacent tendon line segments).

Modified contact element internal force—The penalty method is employed to enforce the contact constraint. The internal force vector needs to be derived to enforce force equilibrium and to evaluate the tangential stiffness matrix of the contact element. The element displacement vector (d_{ct}^e) of the contact element e is defined as

$$d_{ct}^e = (d_{sx}^e \quad d_{sy}^e \quad d_{1x}^e \quad d_{1y}^e \quad d_{1\theta}^e \quad d_{2x}^e \quad d_{2y}^e \quad d_{2\theta}^e \quad d_{3x}^e \quad d_{3y}^e \quad d_{4x}^e \quad d_{4y}^e)^{\mathrm{T}} \tag{7}$$

The first two master nodes (nodes from adjacent embedding elements) of the contact element inherit three degrees of freedom from the nodes of embedding elements. The remaining nodes have two degrees of freedom from the 2-D truss elements. The embedding element is modeled by a very stiff Euler-Bernoulli beam element that shares the nodes of the reinforced concrete beam element and the tendon sheathing element, as shown in Fig. 2. Therefore, the displacement vector comprises 12 degrees of freedom. The N^e, N_0^e, T^e, and T_0^e matrixes are, respectively, defined as

$$N^e = \begin{bmatrix} n & 0 & -(1-\bar{\xi})n & 0 & 0 & -\bar{\xi}n & 0 & 0 & 0 & 0 & 0 & 0 \end{bmatrix}^{\mathrm{T}} \tag{8}$$

$$N_0^e = \begin{bmatrix} 0 & 0 & -n & 0 & 0 & n & 0 & 0 & 0 & 0 & 0 & 0 \end{bmatrix}^{\mathrm{T}} \quad (9)$$

$$T^e = \begin{bmatrix} t & 0 & -(1-\bar{\xi})t & 0 & 0 & -\bar{\xi}t & 0 & 0 & 0 & 0 & 0 & 0 \end{bmatrix}^{\mathrm{T}} \quad (10)$$

$$T_0^e = \begin{bmatrix} 0 & 0 & -t & 0 & 0 & t & 0 & 0 & 0 & 0 & 0 & 0 \end{bmatrix}^{\mathrm{T}} \quad (11)$$

Equations (4) and (5) are recast as

$$\delta g_n^{\ e} = \delta d_{ct}^{\ e\mathrm{T}} N^e \quad (12)$$

$$\delta g_t^{\ e} = \delta d_{ct}^{\ eT} \left(T^e + \frac{g_n^e}{l_{ct}^e} N_0^e + \frac{g_t^e}{l_{ct}^e} T_0^e \right) = \delta d_{ct}^{\ eT} \hat{T}^e \quad (13)$$

The discretized virtual work form of contact contribution without correction force is written as

$$\delta g_n^e P_n^e + \delta g_t^e T_t^e = \delta d_{ct}^{e\mathrm{T}} (N^e P_n^e + \hat{T}^e T_t^e) \quad (14)$$

$$\hat{T}^e = T^e + \frac{g_n^e}{l_{ct}^e} N_0^e + \frac{g_t^e}{l_{ct}^e} T_0^e \quad (15)$$

As illustrated in Fig. 3, a small force along the contact master segment needs to be introduced to correct the normal contract force vector. The corrected unit normal vector n' is computed as

$$n' = \frac{X_3 - X_s + X_4 - X_s}{\left\| X_3 - X_s + X_4 - X_s \right\|} \text{ if } X_3 - X_4 \neq 0 \quad (16)$$

$$n' = \frac{X_4 - X_s}{\left\| X_4 - X_s \right\|} \begin{bmatrix} 0 & 1 \\ -1 & 0 \end{bmatrix} \text{ if } X_3 - X_4 = 0 \quad (17)$$

The tangent between n and n' is obtained as

$$\tan(\alpha) = \frac{\left\| n' \times n \right\|}{n' \cdot n} \frac{n' \cdot t}{\left| n' \cdot t \right|} \quad (18)$$

where α is the angle measured between n and n' clockwise. In the case of n and n' are orthogonal, tan(α) is replaced with a sufficient large value in the iteration. Note that using a finer mesh in the region of large tendon curvature eliminates this numerical difficulty. In the case of t and n' are orthogonal, tan(α) is set to zero.

From Fig. 3, the magnitude of correction force is obtained by the product of the uncorrected normal contact force and absolute value of the tangent. The result obtained from the aforementioned kinematic relation of tangential motion can be then used to construct the correction term in the discretized virtual work form. The discretized form of virtual work with the correction term is expressed as

$$\delta g_n^e P_n^e + \delta g_t^e P_{n\_cor}^e + \delta g_t^e T_t^e = \delta d_{ct}^{e\mathrm{T}} (N^e P_n^e + \hat{T}^e P_{n\_cor}^e + \hat{T}^e T_t^e) \quad (19)$$

$$P_{n\_cor}^e = P_n^e \left| \tan(\alpha) \right| t' \quad (20)$$

where t' is the unit direction vector for correction force.

Equation (19) yields the contact element force vector (G^e) as

$$G_{ct}^e = N^e P_n^e + \hat{T}^e P_{n\_cor}^e + \hat{T}^e T_t^e \quad (21)$$

Constitutive relations at contact interface—A PT beam with perfectly bonded tendons is the simplest case to begin the discussion. All the tendon nodes are constrained at their initial position in the local coordinates of the sheathing elements. Therefore, two equality constraints ($g_n^e = 0$ and $g_t^e = 0$) are enforced in the finite element discretization. The penalty method was employed in this study to impose these constraints. Two large penalty stiffness ε_n and ε_t are selected to compute the normal and tangential contact forces, respectively. The penalty factors are set to values with orders of magnitude larger than the typical stiffness in the system such that the erroneous normal penetration and tangential slip are miniscule compared to overall structural deformation. For a perfectly bonded tendon system, stick behavior (as opposed to slip behavior) is observed in the tangential direction. Thus, the contact forces are determined by the penalty method in both normal and tangential directions. For the stick behavior, the normal and tangential contact forces are given by

$$P_n^{\ e} = \varepsilon_n g_n^{\ e} a^e \quad (22)$$

$$T_t^e = \varepsilon_t g_t^e a^e$$

where a^e is the contact surface within the element that is equal to the length of the master contact segment. For multiple slave nodes in contact with one master segment, a^e is taken proportionally for each contact element e from the total length of master segment based on a tributary area approach.

For perfectly and partially unbonded systems, sliding occurs at the contact interface. The tangential contact force is governed by the integration of the friction law. The Coulomb model of friction was employed, which assumes that the maximum tangential contact pressure is proportional to the normal contact pressure. The stick and slip behavior described by the Coulomb model is stiff and leads to mathematical difficulty. Wriggers (2008) proposed a treatment by splitting the tangential motion into elastic (stick) and plastic (slip) portions. Once the slip condition is fulfilled, an updating algorithm is used to update the total slip distance and tangential contact stress at each time increment as

$$^{i+1}g_t^e = {}^i g_t^e + \frac{\left(\left| {}^{i+1}T_{t\_tr}^e \right| - \mu P_n^e \right) {}^{i+1}t_{t\_tr}^e}{\varepsilon_T} \quad (23)$$

$$^{i+1}T_t^e = \mu P_n^{\ e}\ {}^{i+1}t_{t\_tr}^e$$

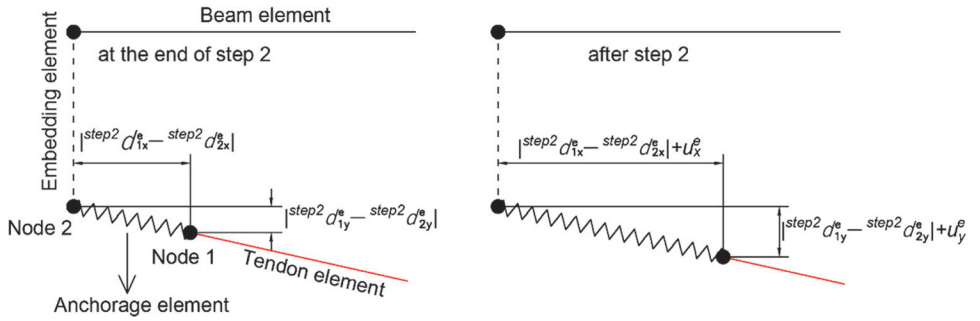

Fig. 4—Formulation of anchorage element.

where ${}^{i+1}g_t^e$ is the updated total slip distance of the slave node in contact element e at time $i + 1$; ${}^{i+1}T_t^e$ is the updated tangential contact stress at time $i + 1$; ${}^{i+1}T_{t\_tr}^e$ is the trial tangential contact stress obtained by assuming a stick behavior at time $i + 1$; μ is the frictional coefficient defined at the contact interface; and ${}^{i+1}t_{t\_tr}^e$ is the slip direction computed at time $i + 1$. Note that the updating algorithm is also a recursive process from time i to $i + 1$, where Eq. (23) is repeatedly computed to update contact element force vector along with other element force vectors at time $i + 1$ until convergence criteria are satisfied.

Tangential stiffness matrixes for normal and tangential contact—The developed finite element program employs Newton-Raphson method to solve the nonlinear equations, which requires linearization of the governing equation. In this study, the tangential stiffness matrix of contact element is numerically evaluated by the complex variable differentiation method (Squire and Trapp 1998). This method is not subject to subtraction error, from which conventional finite difference method usually suffers.

Anchorage element

Jacking procedures—The anchorage element is developed to serve as an interface element between a tendon element and an embedding element. This element is only activated after the completion of tendon jacking and the subsequent anchorage wedge setting. The anchorage element behaves as a very rigid spring between the anchor point and the ends of tendon, as shown in Fig. 4.

The translational motions of Node 1 and Node 2 are constrained to be equal by penalty method. The penalty factor needs to be sufficiently large to eliminate any relative motion between the end of tendon and the corresponding anchor point. A typical finite element simulation is divided into four steps as follows: 1) stretching tendon (friction loss along stretching path of tendon profile); 2) anchorage wedge setting (reversed friction loss); 3) anchoring tendon; and 4) service loading. At Steps 1 and 2, the two degrees of freedom of tendon node (for example, Node 1 in Fig. 4) are set to essential boundary conditions, and the corresponding prescribed displacements and loads are, respectively, applied to emulate the motions of tendon jacking and successive anchorage slip. At each iteration process, the reaction forces are computed at the end node of the tendon and are transmitted to the embedding element node connecting to the tendon (for example, Node 2). This treatment ensures

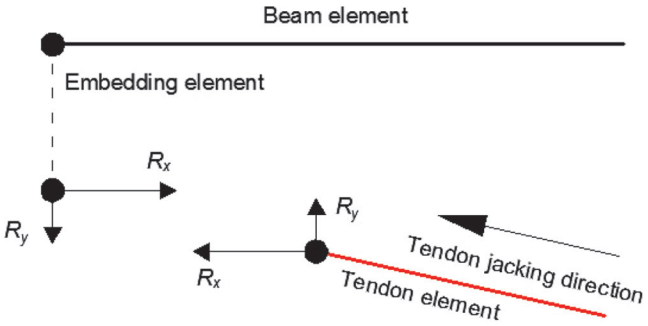

Fig. 5—Tendon jacking reactions transferred to PT member.

that the approximated reactions due to jacking at the end are transmitted to the PT beam. The schematic view of this process is shown in Fig. 5.

Once equilibrium is reached at the end of Step 2, the distance between the end node of the tendon and the node of the corresponding embedding element supposes to be miniscule. The distance is minimized by computing the desired tendon jacking length and anchorage slip in advance. The precomputed displacements are used to determine the initial position of the end node of the tendon. However, at the end of Step 2, a tiny distance may still exist between the end node of the tendon and the corresponding anchor point due to the difficulty of accurately determining the initial position. The distance between Node 1 and Node 2 at the end of Step 2 is accordingly defined as the initial length of anchorage element (Fig. 4). The components of this length in x- and y-axes of global coordinates are, respectively, depicted as $\left|{}^{step2}d_{1x}^e - {}^{step2}d_{2x}^e\right|$ and $\left|{}^{step2}d_{1y}^e - {}^{step2}d_{2y}^e\right|$ in Fig. 4, where ${}^{step2}d_{ac}{}^e$ is the displacement of anchorage element at the end of Step 2. At the beginning of Step 3, anchorage element is activated between the prestressing tendon and corresponding embedding element. In the case of one end jacking, only one anchorage element is activated. Otherwise, two anchorage elements are activated simultaneously for two-end jacking. In addition, the essential boundary condition at the end node of tendon and the corresponding reaction forces at anchor point are removed at the beginning of Step 3. Because the stiffness of added anchorage elements is sufficiently large (at least one order of magnitude larger than the typical stiffness in the system), the relative motions are negligible once the equilibrium is reached at the end of Step 3. After Step 2, the incremental displacements at Node 1 is denoted as u. Therefore, the displacement of Node 1 comprises two parts:

1) initial displacement obtained at the end of Step 2; and 2) the sequential increment after Step 2.

The anchorage element consists of two nodes. The first node is the end node of the tendon and the second node is part of the embedding element at member ends. The displacement vector (d_{ac}^{e}) of an anchorage element is written as

$$d_{ac}^{e} = [d_{1x}^{e} \quad d_{1y}^{e} \quad d_{1\theta}^{e} \quad d_{2x}^{e} \quad d_{2y}^{e} \quad d_{2\theta}^{e}]^{\mathrm{T}} \tag{24}$$

where e denotes the element label. The relative motion between the end node of the tendon and the corresponding node of the embedding element is denoted in global Cartesian coordinates as

$$u_{ac}^{e} = [u_{x}^{e} \quad u_{y}^{e}] \tag{25}$$

At the end of Step 2, the displacement vector of the anchorage element is defined as

$${}^{step2}\bar{d}_{ac}^{e} = {}^{step2}[d_{1x}^{e} \quad d_{1y}^{e} \quad d_{1\theta}^{e} \quad d_{2x}^{e} \quad d_{2y}^{e} \quad d_{2\theta}^{e}]^{\mathrm{T}} \tag{26}$$

According to the definition, u_{ac}^{e} is recast as

$$u_{ac}^{e} = (d_{ac}^{e} - {}^{step2}\bar{d}_{ac}^{e})^{\mathrm{T}} N_{ac} \tag{27}$$

$$N_{ac} = \begin{bmatrix} 1 & 0 & 0 & -1 & 0 & 0 \\ 0 & 1 & 0 & 0 & -1 & 0 \end{bmatrix}^{\mathrm{T}} \tag{28}$$

If the penalty form is employed, the virtual work of an anchorage element e is written as

$$\delta\prod = \varepsilon_{ac} u_{ac}^{e} N_{ac}^{\mathrm{T}} \delta d_{ac}^{e} \tag{29}$$

where ε_{ac} is the penalty factor of anchorage element. The element force vector is obtained as

$$G_{ac}^{e} = (\varepsilon_{ac} u_{ac}^{e} N_{ac}^{\mathrm{T}})^{\mathrm{T}} \tag{30}$$

Substituting Eq. (27) into Eq. (30) yields

$$G_{ac}^{e} = \left[\varepsilon_{ac}(d_{ac}^{e} - {}^{step2}\bar{d}_{ac}^{e})^{\mathrm{T}} N_{ac} N_{ac}^{\mathrm{T}}\right]^{\mathrm{T}} \tag{31}$$

Because the anchorage element has an initial displacement field and behaves nonlinearly, linearization of Eq. (29) leads to the tangential stiffness matrix (k_{ac}^{e})

$$k_{ac}^{e} = \varepsilon_{ac} N_{ac} N_{ac}^{\mathrm{T}} \tag{32}$$

Other element techniques

A brief summary of other element techniques is given in Appendix B. The engineering elements presented in Appendix B are based on the conventional small deformation formulation taking into account the material nonlinearity. A more detailed description is given by Huang (2012).

Solution schemes and implementations

The global tangential stiffness matrix is assembled from the abovementioned five elements as

$$K = K_{ct} + K_{ac} + K_{beam} + K_{emb} + K_{truss} \tag{37}$$

where K_{ct}, K_{ac}, K_{beam}, K_{emb}, and K_{truss} are assembled from element tangential stiffness matrixes k_{ct}^{e}, k_{ac}^{e}, k_{beam}^{e}, k_{emb}^{e}, and k_{truss}^{e} for contact, anchorage, beam, embedding, and truss elements, respectively.

The Newton-Raphson scheme with line search modification was adopted and implemented to solve the nonlinear equations. The partition method was selected to properly impose boundary conditions. The convergence criteria are associated with the l_2 norm of displacement increment vector and residual force vector. A nonlinear finite element code was developed in MATLAB (2010) to implement the proposed formulations. The developed code is available in the first author's PhD dissertation (Huang 2012).

NUMERICAL STUDIES

Analytical solution of curvature-induced prestress loss

The Post-Tensioning Institute (PTI 2006) and ACI Committee 423 (2016) suggest an analytical formula to compute curvature-induced prestress loss as shown in Eq. (38)

$$T_x = T_0 e^{-(\mu\alpha + kx)} \tag{38}$$

where T_x is the post-tensioning force at a distance x along the tendon profile from the jacking end; T_0 is the post-tensioning force at the jacking end; μ is the curvature coefficient which is in the range of 0.05 to 0.3, depending on sheathing material; α is the total angular change in radian at a distance x from the jacking end; and k is the wobble coefficient per foot of tendon that has a range of 0.0001 to 0.0015, depending on sheathing material. This formula was used to compute the analytical solutions with and without wobble effect. The results are compared with numerical solutions in the following examples.

Prestress loss without wobble effect

An imaginary PT beam is studied in this analysis (Fig. 6). The imaginary PT beam is simply supported at a span of 15.2 m (49 ft 10 in.). The rectangular beam section is 254 mm (10 in.) wide and 1016 mm (3 ft 6 in.) deep. It is only reinforced by a single Grade 270 seven-wire strand with an area of 987 mm^2 (1.53 in.^{2}). The tendon profile is draped with zero eccentricity at both ends and with 279 mm (11 in.) eccentricity at midspan. The tendon is unbonded and post-tensioned to an effective prestress of 1407 MPa (204 ksi) (considering friction). Concrete compressive and tensile strengths are, respectively, 27.6 MPa (4 ksi) and 3.3 MPa (480 psi).

The baseline finite element model is discretized by 20 beam elements, 21 embedding elements, 21 truss elements, 20 contact elements, and an anchorage element. Another two models were also constructed with 40 and 60 beam elements to study mesh sensitivity (other elements were also proportionally refined). The wedge setting was selected to be 0.5 mm (0.02 in.) in this case to clearly render the reversal

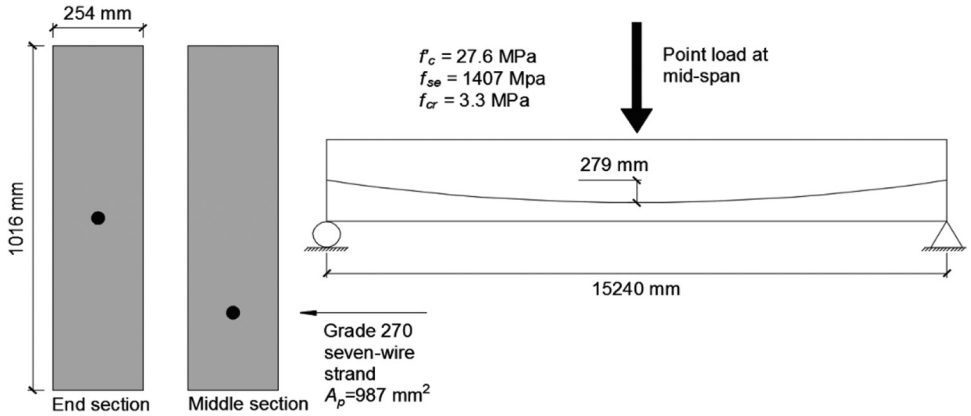

Fig. 6—Details of imaginary simply supported PT beam. (Note: 1 MPa = 0.145 ksi; 1 mm = 0.0394 in.; 1 m = 39 in.; 1 mm^2 = 0.00155 in.^{2}.)

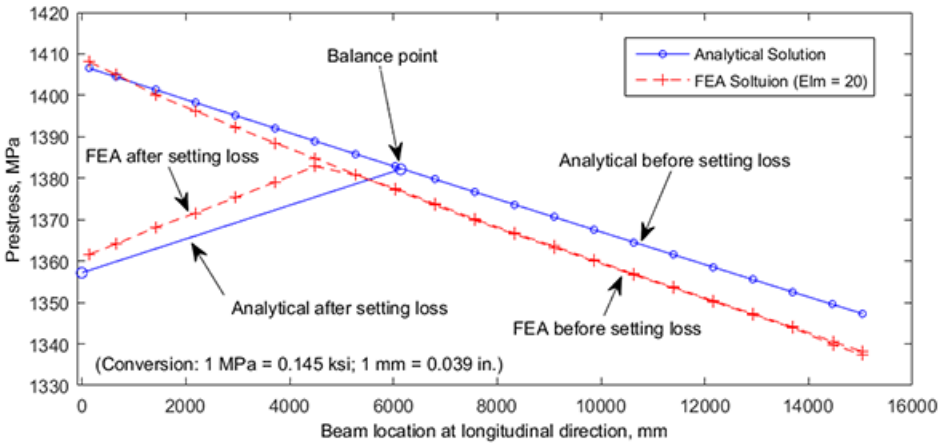

Fig. 7—Comparison of prestress losses before and after wedge setting between FEA and analytical solutions with μ = 0.3 and k = *0.*

of tendon friction within the span (typical wedge setting loss is much larger). The frictional coefficient μ is assumed to be 0.3 for the analytical and numerical models, which yields a partially bonded interface in the simulation. The wobble effect was neglected (k = 0) in the first numerical study.

The frictional loss obtained from the finite element analysis (FEA) is 68.4 MPa (9.9 ksi) at the non-jacking (fixed) end. The analytical prestress loss along the beam is also plotted in Fig. 7. The reverse movement of tendon due to wedge setting leads to prestress loss at the jacking end. The prestress loss starts from the jacking end and is reversed at the balance point (that is, where the reversal of tendon friction occurs). Beyond that point, prestress loss due to wedge setting loss is not present. The model performed quite well to simulate the trend of prestress loss as well as to capture the prestress distribution pattern. Negligible difference exists among solutions with different mesh sizes, which implies that a converged solution is rendered with a relatively coarse mesh (Fig. C1 of Appendix C). The computed prestress losses along with FEA predictions are summarized in Table 1.

Prestress loss with wobble effect

The prestress losses caused by the profile curvature and wobble effect are the curvature-induced friction. The curvature of tendon comprises the intended part (tendon profile) and the unintended part (tendon wobble). The wobble effect is usually assumed to be uniformly distributed along the tendon length direction and its magnitude is characterized by an empirical wobble coefficient k. In this example, the assumed k (for analytical solution) is converted into additional equivalent tendon curvatures by introducing a sinusoidal waveform superposed on the existing tendon profile. The period and magnitude of the sinusoidal function was adjusted such that the total angular change along the profile length equals $(\mu\alpha + kx)/\mu$, where μ and k are used to compute analytical solution. On the other hand, the FEA uses the same frictional coefficient μ. This physical treatment ensures the solutions obtained from FEA are comparable to the analytical solutions. The idealized tendon profile and the adjusted tendon profile for the following studies are shown in Fig. 8 for comparison.

Two continuous two-span PT beams tested by Burns et al. (1991) were selected to evaluate the proposed formulation with wobble effect and to investigate prestress redistribution. Both specimens are continuous over two equal spans at 7.6 m (25 ft). The specimens are pin-supported at middle and roller-supported at both ends. The rectangular sections of both specimens share the same 305 mm (1 ft) width, and are 355 mm (1 ft 2 in.) and 560 mm (1 ft 10 in.) deep, respectively. Both specimens were post-tensioned at one end (south end)

Table 1—Comparison of prestress losses

	Prestress loss* jacking end (analytical)	Prestress loss* jacking end (FEA)	FEA/analytical	Prestress loss* fixed end (analytical)	Prestress loss* fixed end (FEA)	FEA/analytical
Imaginary beam Wedge set = 0.5 mm	3.5%	3.2%	0.92	4.2%	4.9%	1.16
Specimen 1 Wedge set = 1.27 mm (Burns et al. 1991)	5.5%	5.6%	1.02	8.2%	8.2%	1.00
Specimen 2 Wedge set = 1.27 mm (Burns et al. 1991)	6.3%	7.1%	1.13	11.5%	11.1%	0.96
Specimen 1 Wedge set = 3.18 mm (Burns et al. 1991)	9.5%	9.6%	1.01	8.2%	8.3%	1.01
Specimen 2 Wedge set = 3.18 mm (Burns et al. 1991)	10.5%	11.3%	1.08	11.5%	11.1%	0.96

*Prestress loss is computed as ratio of current prestress to effective measured prestress at jacking end.

Note: 1 mm = 0.0394 in.

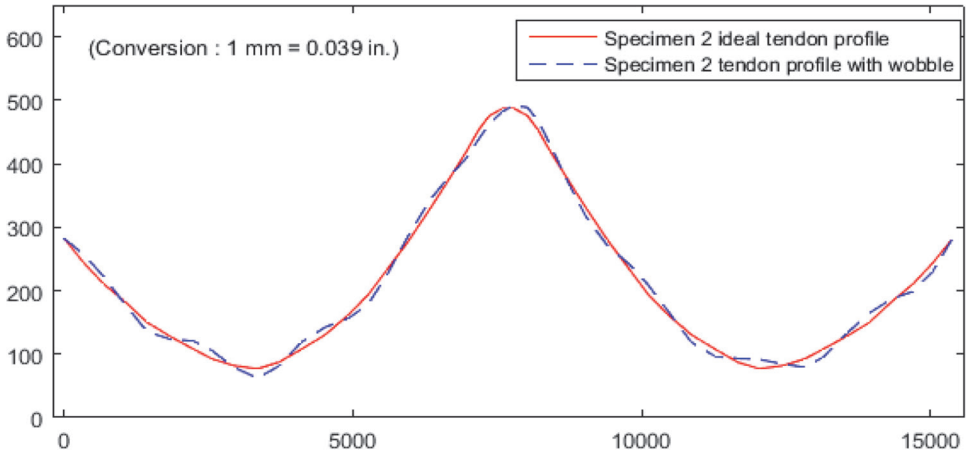

Fig. 8—Comparison of ideal tendon profile to adjusted tendon profile with k = *0.001.*

to an effective stress of 1396 MPa (202 ksi) (approximately $0.75f_{pu}$, where f_{pu} is the ultimate strength of prestressing tendons) with three unbonded tendons of 12.7 mm (0.5 in.) in diameter. Additional reinforcements were also provided at both top and bottom of the section to comply with ACI minimum reinforcing requirement. Additional details of the experimental program are referred to in Burns et al. (1991).

The finite element models for both specimens are composed of 59 beam elements, 58 embedding elements, 58 truss elements, 59 contact elements, and an anchorage element. The frictional and wobble coefficients were set to 0.07 and 0.001, as suggested by Burns et al. (1991) so as the wedge setting length. Figures 9 and 10 compare the numerical prestress losses with the analytical solutions calculated by Burns et al. (1991) before and after loss of wedge setting. Good agreements are achieved between the numerical solution and the analytical solution, as indicated in Table 1.

The cyclic loading was not simulated because the modeling of advanced material constitutive law is beyond the scope of this study. Instead, two simulations ($\mu = 0.07$ and $k = 0.001$ versus $\mu = 0$ and $k = 0$) with monotonic loading were carried out to investigate the difference of prestress redistribution under frictional and frictionless contact for the second specimen. The specimen was point-loaded at the middle of the north span to a deflection of 76 mm (3 in.). While the difference of prestress redistributions is obvious at ultimate state, as shown in Fig. 11 (deflection at middle of north span = 76 mm [3 in.]), the global flexural behaviors are almost identical through the entire loading path (Fig. 12). It is of interest to note that the curvature-induced frictional effect has little impact on the flexural behavior of the specimen on a global scale. One possible explanation of the aforementioned observation is that the bonding condition of prestressed tendon has little effect on the reduced section stiffness (effective section stiffness) due to crack. Therefore, two numerical simulations exhibited almost identical patterns of stiffness reduction as load was gradually increased. This is also evident as both specimens developed similar cracking patterns after reinforcing bar yielding in the simulations (crack is determined by computing strain at each layer of a section and then is compared to the cracking strain defined by the concrete strain-stress curve; cracked regions are plotted in blue in Fig. 13). Another reason is that the stiffness contributions

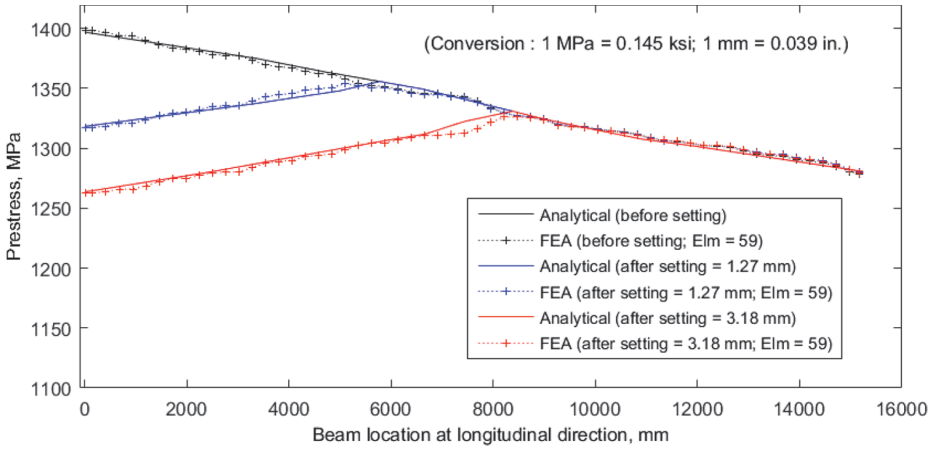

Fig. 9—Comparison of prestress losses between FEA and analytical solutions of Specimen 1. (Note that analytical solutions are reproduced from Burns et al. [1991].)

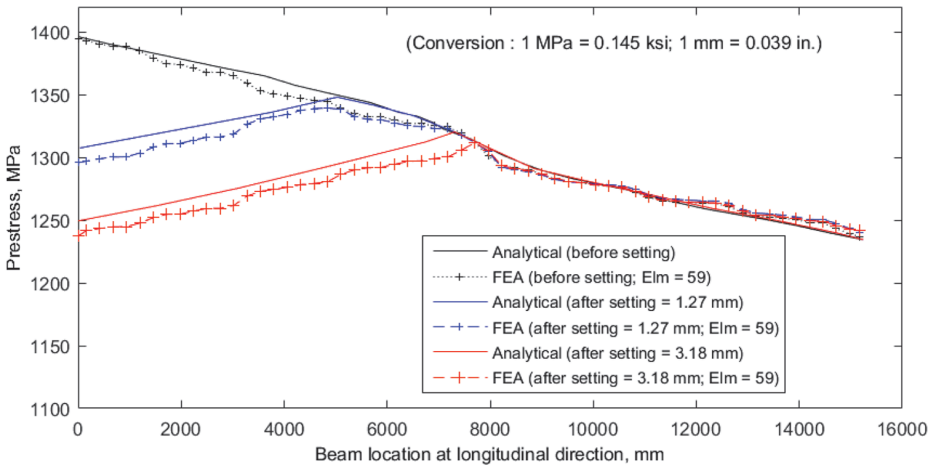

Fig. 10—Comparison of prestress losses between FEA and analytical solution of Specimen 2. (Note that analytical solutions are reproduced from Burns et al. [1991].)

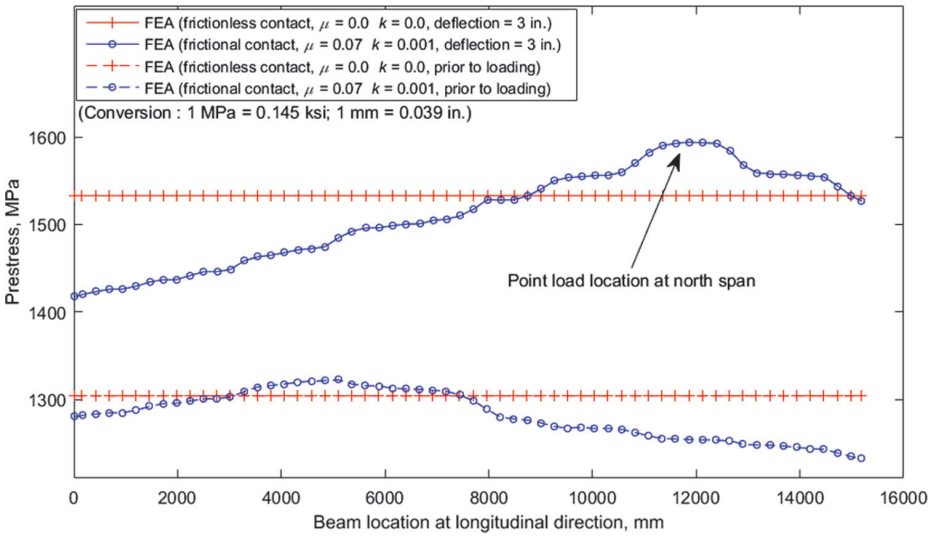

Fig. 11—Comparison of prestress redistribution at ultimate state between frictional and frictionless FEA.

from the prestressed tendons and nonprestressed bars are also similar in either frictionless or frictional contact cases.

Validation using experimental data of PT beams

Five PT beam specimens (A-1, A-2, A-3, A-6, and A-9) tested by Tao and Du (1985) were selected for further

validation. The simply supported PT beams had identical geometries, but were reinforced with different amounts of prestressing tendons and nonprestressed mild steel bars. The sections of rectangular beam were 160 mm (6.3 in.) wide and 279 mm (11 in.) deep. The test specimens with a clear span of 4.2 m (13 ft 9 in.) were subjected to a two-point monotonic loading. The loading points were 1.4 m (4 ft 7 in.) away from each support. The unbonded PT tendons had a straight profile with an effective depth of 220 mm (8.7 in.). The nonprestressed reinforcement layer was only provided at the bottom of the sections with an effective depth of 250 mm (9.8 in.). The detailed description about the test program is referred to in Tao and Du (1985).

The finite element model contains 21 beam elements, 22 embedding elements, 22 truss elements, 21 contact elements, and an anchorage element. The frictional coefficient (μ) is assumed to be 0.3 for the prestressing tendons, which yields a partially bonded interface. The wobble effects were neglected in the simulations. On the other hand, a series of simulations without considering the frictional effects (frictional coefficient μ is zero) were also conducted to identify the influence of the bonding condition on the flexural behavior at a global scale.

Figure 14 (and Fig. C2 of Appendix C) shows the comparisons of the global responses between numerical simulations and the experiments. The simulation results have reasonably good agreements with corresponding experimental data. The cracking and yielding stages of the responses were well captured by the proposed formulation, especially for under-reinforced beams (refer to Fig. 14). As the reinforcement ratio increases, the simulations tend to predict softer responses. This phenomenon was probably caused by the same concrete post-cracking strain-stress relation that was adopted in all the simulations. Tension stiffening effect was reportedly to be a function of the reinforcement ratio (Gilbert 2007). The simulation results can be potentially improved by adopting an advanced tension stiffening model to adjust the strain-stress relation of the RC beam elements at post-cracking stages. Simulations with frictional contact are plotted with cross marks as opposed to frictionless simulations plotted with dotted marks. Again, negligible differences of the global responses were found between the frictional and frictionless contact, which implies the assumption of perfectly unbonded condition is appropriate for modeling small-scale or single-span PT beams with respect to predictions of global flexural responses. However, the solution of stress at local segments of tendons is largely influenced by this simplification, as shown in the previous numerical example (Fig. 11).

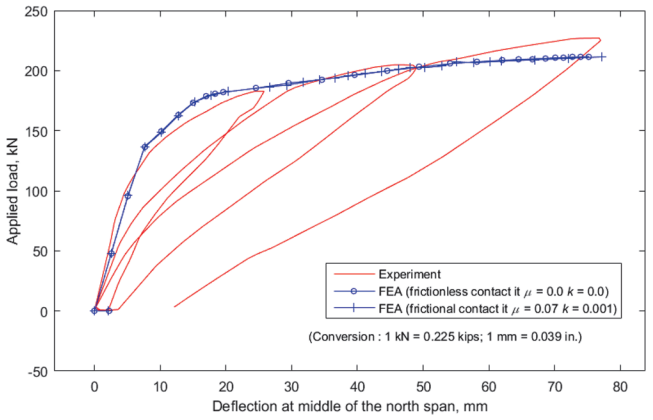

Fig. 12—Comparison of load-deflection curve between FEA and experiment.

Validation using experimental data of PT one-way slabs

Cooke et al. (1981) conducted an experimental investigation of 12 simply supported one-way PT slabs under two-point loading. Two of them (Slab 4 and Slab 5) with unbonded tendons were modeled. Slab 4 and Slab 5 are 3.6 m (11 ft 10 in.) long and are, respectively, 353 mm (1 ft 2 in.) and 705 mm (2 ft 4 in.) wide, with a clear span of 3.4 m (11 ft 7 in.). The thicknesses of both slabs are 180 mm (7 in.). Three straight tendons 12.7 mm (0.5 in.) in diameter were post-tensioned at a constant eccentricity of 120 mm (4.75 in.). Bonded reinforcement was not present in both slabs. More details are in Cooke et al. (1981)

The finite element models for both slabs are composed of the same number of elements and nodes as in the previous numerical study. Only the perfectly unbonded condition (frictional coefficient μ is zero) was investigated. The results of simulations were also compared with an early effort of modeling unbonded tendons made by the authors using a general-purpose finite element analysis package, where the same perfectly unbonded condition was asssumed (Kang et al. 2015).

The global responses are plotted in Fig. 15 (and Fig. C3 of Appendix C). The current finite element formulation

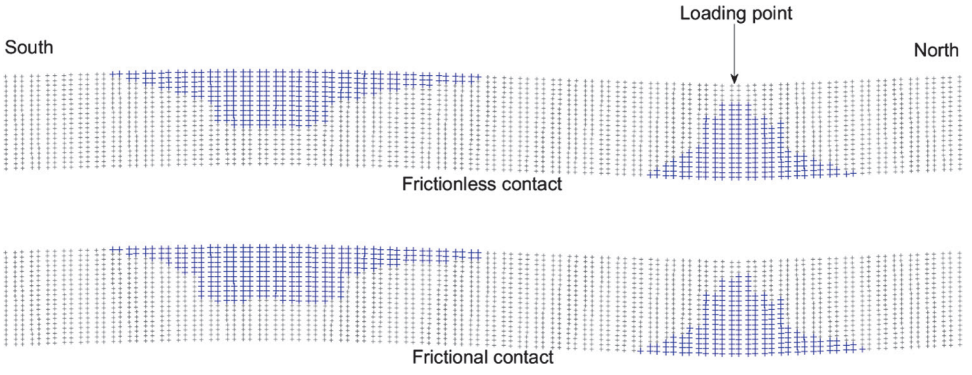

Fig. 13—Comparison of crack patterns between frictional and frictionless FEA. (Note: Specimen depth-to-span ratio is not to scale.)

predicted an accurate flexural response of Slab 4 compared with the experimental result. The simulation of Slab 5 slightly overestimated the yielding strength, as did the previous modeling attempt (Kang et al. 2015). The model, however, accurately captured the trend of bilinear response. The oscillation observed in the previous study was caused by the selected dynamic analysis routine with a combination of dynamic transient response and occurrence of cracking.

SUMMARY AND CONCLUSIONS

An innovative approach to model bonded, partially bonded, and unbonded PT concrete members was developed. The discussion of this study focuses on incorporating a simple contact formulation into conventional engineering elements. The interface of prestressing tendons and corresponding sheathings was modeled through the modified node-to-segment contact formulation. Several types of elements are discussed in depth and developed to emulate behaviors of PT beams. The proposed finite element formulation was implemented into a nonlinear finite element code developed by the authors in MATLAB. Several numerical studies were carried out to validate the reliability of the modeling. Numerical studies showed its reliability through not only good reproduction of global structural responses, but prestress loss and redistribution at local scale. Furthermore, by using the proposed numerical routines, a design solution can be reached with dispatch, whereas general-purpose nonlinear FEA codes tend to fall short in terms of simplified modeling and design efficiency.

The proposed framework is generic enough to be extended to other studies in the future. For example, the bond stress at tendon-sheathing interface can be further investigated by implementing advanced constitutive models at the contact interface. Additionally, it can be used to analyze other types of PT members such as transfer girders and structural walls besides PT beams and one-way slabs by introducing other types of structural elements.

The other aims of the study included reproducing both global flexural behavior and localized prestress loss/redistribution of unbonded and partially bonded PT members, which allowed for assessment of the effect of local behavior on the global behavior.

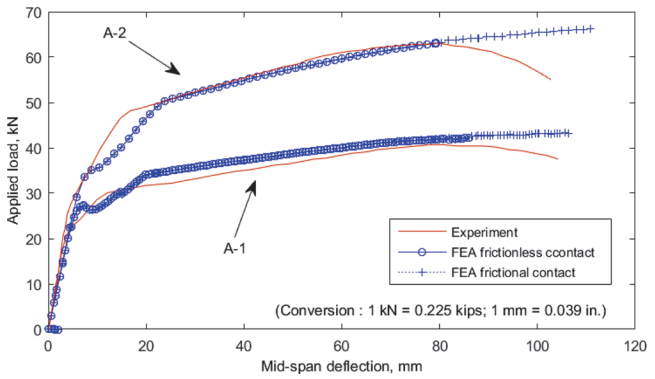

Fig. 14—Global responses of Specimens A-1 and A-2.

AUTHOR BIOS

Yu Huang *is a Structural Engineer at Rosenwasser/Grossman Consulting Engineers, New York, NY. He received his PhD from the University of Oklahoma, Norman, OK. His research interests include the design and analysis of post-tensioned prestressed concrete structures.*

Thomas H.-K. Kang, *FACI, is an Associate Professor at Seoul National University, Seoul, South Korea, and was an Assistant Professor at the University of Oklahoma, Norman, OK. He is a member of ACI Committee 369, Seismic Repair and Rehabilitation; Joint ACI-ASCE Committees 335, Composite and Hybrid Structures; 352, Joints and Connections in Monolithic Concrete Structures; and 423, Prestressed Concrete; as well as Joint ACI-ASME Committee 359, Concrete Containments for Nuclear Reactors. He received the 2009 ACI Wason Medal for Most Meritorious Paper. His research interests include the design and behavior of reinforced, prestressed, and post-tensioned concrete structures.*

ACKNOWLEDGMENTS

The work was funded by the University of Oklahoma and Institute of Engineering Research of Seoul National University.

REFERENCES

ACI Committee 423, 2016, "Guide to Estimating Prestress Losses (ACI 423.10R-16)," American Concrete Institute, Farmington Hills, MI, 64 pp.

Burns, N. H.; Helwig, T.; and Tsujimoto, T., 1991, "Effective Prestress Force in Continuous Post-Tensioned Beams with Unbonded Tendons," *ACI Structural Journal*, V. 88, No. 1, Jan.-Feb., pp. 84-90.

Cooke, N.; Park, R.; and Yong, P., 1981, "Flexural Strength of Prestressed Concrete Members with Unbonded Tendons," *PCI Journal*, V. 26, No. 6, Nov.-Dec., pp. 52-81. doi: 10.15554/pcij.11011981.52.81

El-Mezaini, N.; Balkaya, C.; and Çitipitiolu, E., 1991, "Analysis of Frames with Nonprismatic Members," *Journal of Structural*

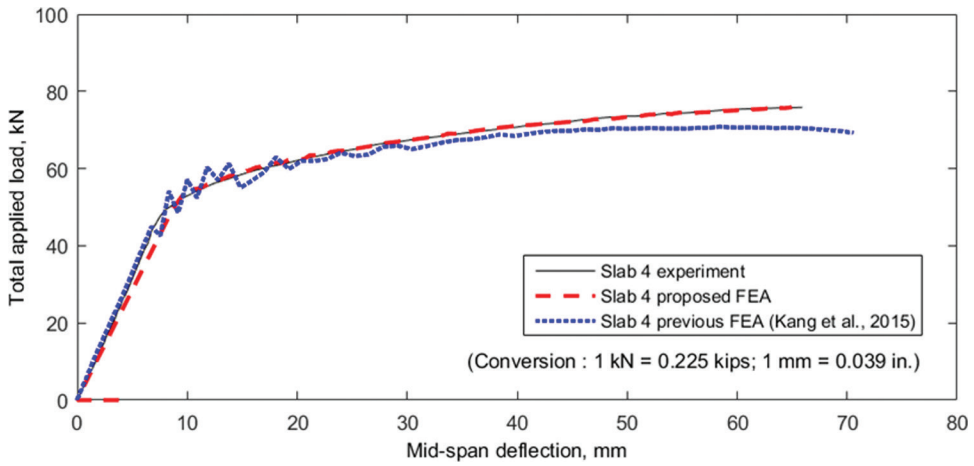

Fig. 15—Global responses of Specimen Slab 4. (Note that previous FEA of Slab 4 was performed using general-purpose finite element analysis package without considering friction effect [Kang et al. 2015].)

Engineering, ASCE, V. 117, No. 6, June, pp. 1573-1592. doi: 10.1061/(ASCE)0733-9445(1991)117:6(1573)

El-Mezaini, N., and Çıtıpıtıolu, E., 1991, "Finite Element Analysis of Prestressed and Reinforced Concrete Structures," *Journal of Structural Engineering*, ASCE, V. 117, No. 10, Oct., pp. 2851-2864. doi: 10.1061/(ASCE)0733-9445(1991)117:10(2851)

Ellobody, E., and Bailey, C. G., 2008, "Testing and Modelling of Bonded and Unbonded Post-Tensioned Concrete Slabs in Fire," 5th International Conference on Structures in Fire, pp. 392-405.

Fagan, E. M.; Leen, S. B.; de la Torre, O.; and Goggins, J., 2017, "Experimental Investigation, Numerical Modelling and Multi-Objective Optimisation of Composite Wind Turbine Blades," *Journal of Structural Integrity and Maintenance*, V. 2, No. 2, June, pp. 109-119.

Gilbert, R. I., 2007, "Tension Stiffening in Lightly Reinforced Concrete Slabs," *Journal of Structural Engineering*, ASCE, V. 133, No. 6, June, pp. 899-903. doi: 10.1061/(ASCE)0733-9445(2007)133:6(899)

Huang, Y., 2012, "Finite Element Method for Post-Tensioned Prestressed Concrete Structures," PhD thesis, University of Oklahoma, Norman, OK, 326 pp.

Huang, Y.; Kang, T. H.-K.; Ramseyer, C.; and Rha, C., 2010, "Background to Multi-Scale Modelling of Unbonded Post-Tensioned Concrete Structures," *International Journal of Theoretical and Applied Multiscale Mechanics*, V. 1, No. 3, pp. 219-230. doi: 10.1504/IJTAMM.2010.033601

Kang, T. H.-K.; Wallace, J. W.; and Elwood, K. J., 2009, "Nonlinear Modeling of Flat-Plate Systems," *Journal of Structural Engineering*, ASCE, V. 135, No. 2, Feb., pp. 147-158.

Kang, T. H.-K.; Huang, Y.; Shin, M.; Lee, J. D.; and Cho, A. S., 2015, "Experimental and Numerical Assessment of Bonded and Unbonded Post-Tensioned Concrete Members," *ACI Structural Journal*, V. 112, No. 6, Nov.-Dec., pp. 735-748. doi: 10.14359/51688194

Kang, Y.-J., and Scordelis, A. C., 1980, "Nonlinear Analysis of Prestressed Concrete Frames," *Journal of the Structural Division*, ASCE, V. 106, Feb., pp. 445-462.

MATLAB, 2010, "Download Manual MATLAB 2010," MathWorks, Natick, MA.

Nikolic, Z., and Mihanovic, A., 1997, "Non-linear Finite Element Analysis of Post-Tensioned Concrete Structures," *Engineering Computations*, V. 14, No. 5, pp. 509-528. doi: 10.1108/02644409710170348

PTI TAB.1-06, 2006, *Post-Tensioning Manual*, sixth edition, Post-Tensioning Institute, Farmington Hills, MI, 254 pp.

Squire, W., and Trapp, G., 1998, "Using Complex Variables to Estimate Derivatives of Real Functions," *SIAM Review*, V. 40, No. 1, pp. 110-112. doi: 10.1137/S003614459631241X

Tao, X., and Du, G., 1985, "Ultimate Stress of Unbonded Tendons in Partially Prestressed Concrete Beams," *PCI Journal*, V. 30, No. 6, pp. 72-91. doi: 10.15554/pcij.11011985.72.91

Van Greunen, J., and Scordelis, A. C., 1983, "Nonlinear Analysis of Prestressed Concrete Slabs," *Journal of Structural Engineering*, ASCE, V. 109, No. 7, July, pp. 1742-1760. doi: 10.1061/(ASCE)0733-9445(1983)109:7(1742)

Vecchio, F. J.; Gauvreau, P.; and Liu, K., 2006, "Modeling of Unbonded Post-Tensioned Concrete Beams Critical in Shear," *ACI Structural Journal*, V. 103, No. 1, Jan.-Feb., pp. 57-64.

Wriggers, P., 2008, *Nonlinear Finite Element Methods*, first edition, Springer, New York, 572 pp.

Wu, X.; Otani, S.; and Shiohara, H., 2001, "Tendon Model for Nonlinear Analysis of Prestressed Concrete Structures," *Journal of Structural Engineering*, ASCE, V. 127, No. 4, Apr., pp. 398-405. doi: 10.1061/(ASCE)0733-9445(2001)127:4(398)